Journal of Materials Chemistry A

PAPER

View Article Online
View Journal | View Issue

Cite this: J. Mater. Chem. A, 2017, 5, 23805

Titanium alkylphosphate functionalised mesoporous silica for enhanced uptake of rare-earth ions†

Wenzhong Zhang, ‡*[a] Dženita Avdibegović, ‡[b] Risto Koivula, [a] Timo Hatanpää, [c] Sami Hietala, [c] Mercedes Regadío, [b] Koen Binnemans *[b] and Risto Harjula§[a]

The separation of rare-earth elements (REEs) is usually carried out by a multi-stage solvent extraction process utilising organophosphorus extractants. Inspired by the structure of the solvating extractant tri-*n*-butyl phosphate (TBP), new sorbents were designed by covalently attaching short *n*-alkyl chains (ethyl, *n*-propyl and *n*-butyl) to titanium(IV) phosphate functionalised mesoporous MCM-41 silica by a layer-by-layer grafting route. Mesoporous MCM-41 silica served as a versatile porous support and the grafted titanium(IV) derivatives provided enhanced acid stability and solvating extraction capability. Various characterisation methods including solid-state ^{13}C, ^{29}Si and ^{31}P magic-angle spinning (MAS) nuclear magnetic resonance (NMR) and simultaneous thermogravimetry and differential scanning calorimetry-mass spectroscopy (TG/DSC-MS) were used to confirm the ligand attachment. The hybrid materials showed a better uptake of rare-earth ions from nitrate feed solution than the unmodified inorganic material. The optimal separation factor (SF) obtained for scandium–lanthanum separation is in excess of 100 000 at pH 2.1. The SFs calculated for dysprosium–neodymium are approximately 3, which is comparable to that of TBP in a typical solvent extraction setup. This study provides a new strategy to design inorganic–organic hybrid sorbents based on the structure of organophosphorus extractants *via* metal(IV)–O–P bonds.

Received 14th September 2017
Accepted 31st October 2017

DOI: 10.1039/c7ta08127h

rsc.li/materials-a

Introduction

Rare-earth elements (REEs) nowadays play an increasing role as critical raw materials for the transition to cleaner energy and the production of high-tech devices.[1] They are used in wind turbines (Nd, Dy, Sm, Pr), hybrid and electric cars (Nd, Dy, La) and lamp phosphors (Eu, Gd, Tb, Yb, La).[2] For these applications, pure REEs are required. Solvent extraction (SX) and ion-exchange are the most important REE separation techniques. However, the separation of complex mixtures of REEs remains challenging owing to the similarity of their chemical properties.[3,4] The SX process involves the use of organic extractants which transfer the REE ions from the aqueous to the organic phase.[5] Usually, the organic phase consists of a diluent (kerosene) to dissolve the extractant, reduce the viscosity of the loaded organic phase and facilitate the hydrodynamics of the extracted species. Tri-*n*-butyl phosphate (TBP) is a classic solvating extractant used in the separation of REE.[6,7] The neutral REE-nitrate complexes are coordinated by the phosphoryl group in TBP, yielding an extractable complex (eqn (1)):[3,8,9]

$$REE^{3+}_{(aq.)} + 3NO_{3(aq.)}{}^{-} + 3TBP_{(org.)} \leftrightarrows [REE(NO_3)_3TBP_3]_{(org.)} \quad (1)$$

The extraction of REEs must be carried out at high nitrate salt concentrations (often > 6 M) to shift the equilibrium in eqn (1) to the right. The separation is based on the slightly different complex stability constants for different lanthanides.[9]

Solid-phase extraction (SPX) is regarded as an alternative for SX.[10–12] Recently, organic–inorganic hybrid materials, including metal phosphonates (metal–organic framework)[13,14] and ligand-functionalised silica (phosphine oxide,[15] phosphonates[16–18] and diglycolamide-derivatives[19–22]) have been developed as adsorbents for REE separation. The major advantage of SPX over SX is the elimination of one of the liquid phases.[2]

Selective ion-exchange materials, which are used in SPX, take advantage of the differences in the acidity and ionic radii of REEs. Solid metal(IV) phosphates are a class of inorganic ion-exchange materials with a good stability against strong acids and a good thermal stability.[23] Some of us have recently shown

[a]Department of Chemistry – Radiochemistry, FI-00014 University of Helsinki, P.O. Box 55, Finland. E-mail: Wenzhong.Zhang@helsinki.fi
[b]Department of Chemistry, KU Leuven, Celestijnenlaan 200F, P.O. Box 2404, B-3001 Heverlee, Belgium. E-mail: Koen.Binnemans@kuleuven.be
[c]Department of Chemistry, FI-00014 University of Helsinki, P.O. Box 55, Finland

† Electronic supplementary information (ESI) available: Detailed characterisations. See DOI: 10.1039/c7ta08127h

‡ These two authors contributed equally to this work.

§ Deceased, September 11, 2017.

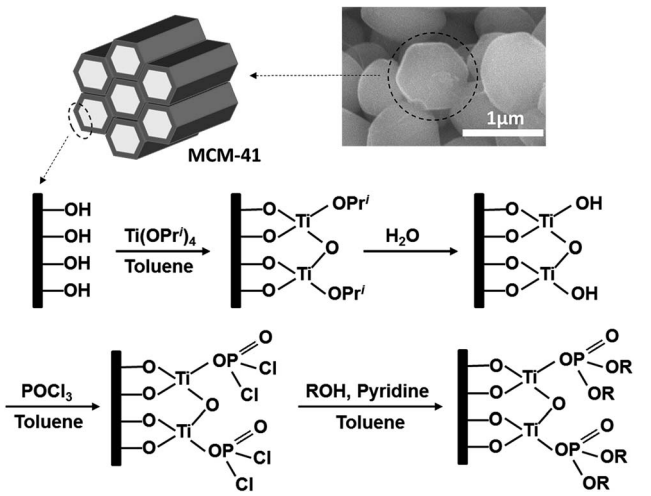

Scheme 1 Layer-by-layer synthesis route of M41 silica functionalised titanium(IV) *n*-alkylphosphate materials (R = H, Et, *n*-Pr and *n*-Bu).

that titanium phosphates are useful for scandium recovery from acidic media due to metal affinity towards the phosphate ligands and size selection.[24] However, one major drawback of these metal phosphates is the high framework density due to their densely packed layered structure, which leads to a relatively low surface area and slow kinetics. Decorating a porous support with metal phosphate could mitigate this issue. Silica materials are especially suitable to this end since they offer tuneable framework structures with high surface area. The mesoporous MCM-41 (M41) silica[25] consists of an ordered hexagonal pore array built up by unidimensional and hexagonal pores.[26] Many silanol groups are available on the surface of the pores, permitting post-synthetic functionalisation of the heteroatoms.

A solution-based layer-by-layer deposition has been developed to graft amorphous titanium phosphate onto silica.[27–29] The resulted grafted material showed enhanced metal uptake compared to that of pure silica support or to that of metal phosphate. The introduction of titanium also improves the acid stability of the phosphate group since direct Si–O–P linkages are prone to hydrolysis.[30]

Herein, we present the conceptual design and synthesis of a hybrid SPX material composed of M41 silica as a support and titanium(IV) alkylphosphate covalent grafts as the functional groups (Scheme 1). The basicity of P=O groups is expected to be influenced by titanium(IV) and the organic *n*-alkyl chain lengths can impose steric effects[10] to facilitate molecular recognition events.[31] The surface alkylphosphate groups mimicking the TBP structure showed good performance for uptake of rare-earth nitrate complexes in acidic solutions using ammonium nitrate as the source of nitrate ions.

Experimental

Chemicals

Titanium(IV) isopropoxide (Ti(OPr^i)$_4$, >97%), tetraethyl orthosilicate (TEOS, >98%), hexadecyltrimethylammonium bromide (CTAB, >99%), neodymium(III) nitrate hexahydrate (>99.9%), dysprosium(III) nitrate hydrate (>99.9%) and ammonia solution (25 wt%) were purchased from Sigma-Aldrich (Helsinki, Finland). Pyridine (>99%), ethanol (>99.5%), *n*-propanol (>99.0%) and *n*-butanol (>99.4%) were purchased from Fisher Chemical (Helsinki, Finland). Scandium(III) oxide (>99.99%) were acquired from Alfa Aesar (Helsinki, Finland). Phosphorus oxychloride (>99%) was obtained from ACROS Organics (Helsinki, Finland). Ammonium nitrate was obtained from Riedel-de Haen GmbH (Seelze, Germany). All elemental (P, Dy, La, Nd, Sc, and Ti) single standard solutions (1000 mg L^{-1}, PrimAg-plus cert. ref. material) and nitric acid (SpA super purity, 67–69%) were purchased from Romil (Cambridge, UK). Milli-Q water (Millipore) with a resistivity of 18.2 MΩ cm was used throughout the experiments.

Synthesis of silica support

M41 silica was synthesised according to a literature procedure.[32] At first, 2.0 g of CTAB was dissolved in a diluted ammonia solution (205 mL of 25 wt% ammonia solution mixed with 270 mL of H_2O). Subsequently, 10 mL of TEOS was added dropwise to the solution, giving rise to a white slurry. The slurry was then aged for 2 h before harvested by filtration and washing. To remove the template, the final product was calcined in air at 550 °C. The molar composition of the precursor was 525 H_2O: 69 NH_4OH: 0.125 CTAB: 1 TEOS.

Grafting of titanium(IV) alkylphosphate

The synthesis was carried out under argon atmosphere. In a typical experiment, 1 g of M41 was mixed with 20 mL of dry toluene in a two-neck flask sealed with a rubber septum, to which 3.4 mmol of Ti(OPr^i)$_4$ was added through a syringe at room temperature. The slurry was stirred and refluxed at 80 °C for 2 h. The obtained solid was washed three times with toluene to remove unreacted Ti(OPr^i)$_4$ precursor, washed again three times with water to hydrolyse the alkoxy groups and then dried in air at 80 °C. The modification of the phosphate groups was achieved by repeating the same procedure using 10.2 mmol of $POCl_3$ (except for the washing step). The obtained solid was then washed three times with 20 mL of toluene. The alkyl chains were attached to the material through esterification reactions by corresponding alcohols. To a sealed two-neck flask, 20 mL of toluene was added together with the toluene-washed slurry. The mixture was stirred and the flask was cooled in an ice-water bath before slowly adding 30 mmol of pyridine and, afterwards, 60 mmol of alcohol (ethanol, *n*-propanol or *n*-butanol). After the addition was completed, the reaction mixture was heated slowly to 80 °C and held there for 2 h. The products were washed three times with 20 mL of acetone and three times with 20 mL of water before drying in vacuum at 50 °C. The final products are denoted as M41-TiEtP, M41-TiPrP and M41-TiBuP corresponding to ethyl-, *n*-propyl- and *n*-butyl-grafted materials, respectively. For comparative reasons, the inorganic titanium(IV) phosphate grafted M41 (denoted as M41-TiP) was also synthesised by direct hydrolysing the product with water after the reaction with $POCl_3$.

Characterisation

The surface morphology was examined using a Hitachi S-4800 FE-SEM (field-emission scanning electron microscopy) after coating with a 3 nm-thick layer of Pd–Au by sputtering. Powder X-ray diffraction (XRD) patterns were collected using a PANalytical X'Pert PW3710 MPD diffractometer coupled with a PW3020 vertical goniometer in Bragg–Brentano geometry. X-ray radiation was sourced from monochromatic CuKα line (λ = 1.54056 Å) at 40 kV and 40 mA. All solid-state magic angle spinning (MAS) nuclear magnetic resonance (NMR) spectra were acquired on a Bruker Avance III 500 MHz spectrometer equipped with 4 mm H/X/Y MAS probe. The samples were filled in a 4 mm ZrO_2 rotor and measured under MAS at 12 (for ^{29}Si) and 15 kHz (for ^{1}H, ^{13}C and ^{31}P). The ^{1}H spectra were acquired with a 90° pulse (83 kHz RF pulse), 5 s recycle delay and 64 scans. All the ^{1}H spectra were referenced to the secondary ^{1}H reference adamantane (^{1}H peak at 1.773 ppm), which was referenced to the primary reference tetramethylsilane (TMS) at 0 ppm. ^{13}C spectra were recorded with ^{1}H–^{13}C cross-polarisation pulse sequence, 2048 scans, recycle delay of 5 s, spinal-64 ^{1}H decoupling and a contact time 0.5 ms. Line broadening of 50 Hz was applied for spectral processing. The spectra were referenced to the ^{13}C adamantane peak at 38.5 ppm, which was primarily referenced to the TMS peak at 0 ppm. ^{29}Si spectra were obtained with a 4.18 μs pulse, 200 s recycle delay and 256 scans. The spectra were externally referenced also to TMS. ^{31}P spectra were acquired with a 90° pulse (77 kHz RF), 100 s recycle delay and 64 scans. ^{31}P NMR spectra were referenced to the ammonium dihydrogen phosphate peak at 0.8 ppm, which was further referenced to the primary reference 85% H_3PO_4 peak at 0 ppm. Infrared spectra (700–4000 cm^{-1}) were recorded on a Bruker Vertex 70 spectrometer (Bruker Optics) with a platinum ATR single reflection diamond attenuated total reflection (ATR) accessory. The CHN (carbon, hydrogen, nitrogen) elemental contents were analysed by a Thermo Scientific Interscience Flash 2000 Elemental analyser. The textural properties of the materials were determined by N_2 adsorption at 77 K, using a Quanta Chrome NOVA 2200e surface area and pore size analyser. Samples were degassed at 160 °C (M41 and M41-TiP) or at 80 °C (other samples) for 23 h prior to analysis. The BET surface area was calculated by the Brunauer, Emmett, and Teller (BET) method using the adsorption isotherms. Pore-size distributions were calculated using nonlocal density functional theory (NLDFT) with cylindrical silica pores. Simultaneous thermogravimetry and differential scanning calorimetry-mass spectroscopy (TG/DSC-MS) analysis was performed using a simultaneous TG/DSC apparatus (STA 449F3 Jupiter, Netzsch) connected to JAS-Agilent GCMS (7890 GC/MSD5977A). In the dynamic TG measurements, the samples were heated from 30 °C to 800 °C. The heating rate was 20 °C min^{-1}, with a helium flow of 40 mL min^{-1}. A sample of 5 to 10 mg was placed in an open 90 μL alumina crucible. Part of the evolving gas mixture (50%) was led with aid of diaphragm pump through a heated transfer line with silico-steel capillary tubing to a heated gas sampling system (JAS valve), both maintained at 250 °C. From the sampling system on the top of an Agilent GC-MS (7890B GC/MSD5977A), part of the evolved gas mixture was continuously sampled into the GC-MS system. In the GC furnace held at 250 °C there was a 60 cm long GC capillary which acted as a pressure restrictor in front of the MS detector. Data collection was carried out with Agilent MassHunter software.

Calculations

The distribution coefficient (K_d, mL g^{-1}) demonstrates the distribution of an element within the equilibrium solution and solid material. It was calculated by the following equation (eqn (2)):

$$K_d = \frac{[\overline{M^{n+}}]_{eq.}}{[M^{n+}]_{eq.}} = \frac{[M^{n+}]_{i.} - [M^{n+}]_{eq.}}{[M^{n+}]_{eq.}} \times \frac{V}{m} \quad (2)$$

where $[\overline{M^{n+}}]_{eq.}$ is the equilibrium metal concentration in the solid (mg g^{-1}), $[M^{n+}]_{i.}$ and $[M^{n+}]_{eq.}$ are respectively the metal concentration of the solution at initial and equilibrium states (mg mL^{-1}), V is the volume of the solution (mL) and m is the mass of the material (g).

The separation factor (SF) between metal ions M_1 and M_2 was subsequently calculated based on their K_d values (eqn (3)):

$$SF_{M_1/M_2} = \frac{K_d(M_1)}{K_d(M_2)} \quad (3)$$

Batch sorption and desorption experiments

Typically, 50 (±1) mg of material was placed in a polyethylene vial with 20 mL of test solution. Samples were equilibrated overnight on a constant rotary mixer (50 rpm). The solid/liquid separation was then achieved by centrifugation (15 min at 3000*g*), and an adequate amount of the supernatant was filtered through a 0.45 μm PVDF syringe filter for concentration determination. Equilibrium pH was measured from the remaining solution. Two systems were evaluated: in the first system, a 1 mM equimolar mixture of Sc and La (with and without 5 M NH_4NO_3) were studied as a function of pH in the range of 1 to 4. The second system comprised a 1 mM equimolar mixture of Nd and Dy (with 5 M NH_4NO_3), sorption was studied as a function of the pH in the range of 1 to 5. The pH was adjusted with 1 M HNO_3. Desorption experiments were conducted by first loading the materials with metals at appropriate equilibrium pH. After loading equilibrium was reached, the supernatant was decanted. The remaining material was quickly washed three times with 20 mL of acetone using centrifugation and re-dispersion, and the supernatants were all discarded. Note that ammonium nitrate is soluble in acetone. The acquired slurry was dried in an oven at 50 °C. After that, 20 mL of acid solution was introduced into the tube and samples were again equilibrated. Finally, after centrifugation, the supernatant was taken for metal analysis. The desorption solution used here were water, 0.01 M HNO_3 and 0.1 M HNO_3. Cyclic sorption–desorption was performed for five cycles. Acid stability was measured by batch experiments using 0.01 M and 0.1 M HNO_3 with an equilibration time of 6 h.

Determination of metal concentrations was performed on a Perkin Elmer Optima 8300 inductively coupled plasma optical emission spectrometer (ICP-OES) in dual view, with a GemTip

CrossFlow II nebuliser, a Scott Spray Chamber Assembly, a sapphire injector and a HybridXLT ceramic torch. Atomic emission lines were prioritised and possible spectrum interferences were minimised. Lanthanum or praseodymium was used as internal standard and for quality control. Samples were diluted to concentrations below 25 ppm and linear calibration curve was established by 0, 0.5, 1, 2, 5, 10 and 25 ppm standard solutions.

Results and discussion

Synthesis and characterisation

Our synthesis approach is shown in Scheme 1: the M41 silica was grafted with titanium(IV) phosphate *via* 'acid–base pair' precursors utilising $Ti(OPr^i)_4$ and $POCl_3$.[29] The reactivity of the P–Cl bonds was later harnessed for grafting alkoxy groups through reaction with the corresponding alcohol (ethanol, *n*-propanol and *n*-butanol). The reaction was carefully controlled (by drop-wise addition of the alcohol) to avoid the E2 elimination of the alcohol to an alkene. Additionally, HCl generated in the reaction was removed by a base (pyridine).

The FE-SEM images of those hexagonal-shape materials are available in Fig. 1. All functionalised materials contained approximately 8 wt% of Ti and 4 wt% of P (Table 1). The small-angle XRD patterns of grafted hybrid materials showed well-resolved peaks at $2\theta = 3$–$4°$ (Fig. 2), confirming the preservation of the ordered hexagonal mesoporous structure. The slight shift of the [100] diffraction peak to higher diffraction angles represents the decrease of the interplanar spacing (d). It is obvious that the grafted alkyl chains occupy pore spaces and therefore lead to smaller d values (Table 1). However, due to the differences in reactivity and bulkiness of the different alcohols, the reaction yields varied. More ethyl and *n*-propyl groups could be grafted compared to *n*-butyl groups. A similar trend was evident from the N_2 porosimetry results. The nitrogen adsorption–desorption isotherms and pore-size distributions are shown in Fig. S1.† All the materials exhibited type-IV isotherms and very narrow H1 type hysteresis loop, indicating the narrow channels of the M41 silica. The pore-size distribution results were in line with the calculated d_{100} spacing from XRD. The BET surface area decreased from M41 support (1022 $m^2\ g^{-1}$) to M41-TiP (879 $m^2\ g^{-1}$) and then to even lower values when alkyl chains were grafted (Table 1). The Fourier transform infrared (FTIR) spectra of the synthesised materials are shown in Fig. S2.† Two bands centred at 1250 and 1060 cm^{-1} correspond

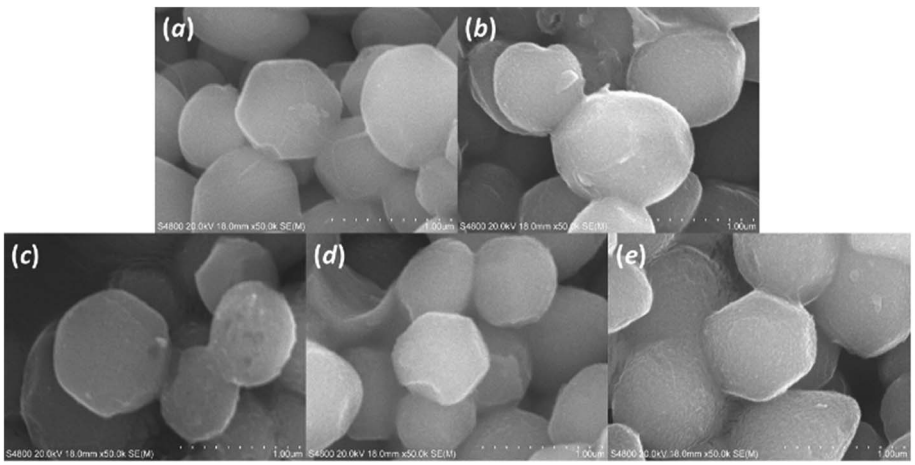

Fig. 1 FE-SEM images of the (a) M41, (b) M41-TiP, (c) M41-TiEtP, (d) M41-TiPrP and (e) M41-TiBuP.

Table 1 Physicochemical properties of the pristine and the grafted M41 materials

Sample[a]	S_{BET}[b] ($m^2\ g^{-1}$)	d_{100}[c] (nm)	V_{total}[d] ($cm^3\ g^{-1}$)	Content[e] wt% Ti	wt% P	mmol g^{-1} Ti	mmol g^{-1} P	Si sites[f] Q^2 sites (%) $(SiO)_2{*}Si(OH)_2$	Q^3 sites (%) $(SiO)_3{*}SiOH$	Q^4 sites (%) $(SiO)_4{*}Si$
M41	1022	3.67	0.76	—	—	—	—	7.4	31.5	61.1
M41-TiP	879	3.54	0.51	8.38	4.04	1.75	1.30	7.3	26.8	65.8
M41-TiEtP	514	3.42	0.29	7.45	3.65	1.56	1.18	7.1	25.3	67.7
M41-TiPrP	443	3.43	0.30	8.09	3.86	1.69	1.24	6.1	32.0	61.8
M41-TiBuP	350	3.47	0.25	7.89	3.65	1.65	1.18	7.4	29.3	63.3

[a] Samples denotation: MCM-41 silica (M41), titanium(IV) phosphate functionalised MCM-41 silica (M41-TiP) and *n*-alkyl chains (Et, Pr, Bu) grafted titanium(IV) phosphate functionalised MCM-41 silica (M41-TiEtP, M41-TiPrP and M41-TiBuP). [b] S_{BET}: BET specific surface area. [c] d_{100}: interplanar distance calculated by diffraction of [100] plane. [d] V_{total}: total pore volume estimated at a relative pressure of 0.99, assuming full surface saturation. [e] Chemical content determined by total digestion. [f] Relative peak areas calculated from the deconvoluted ^{29}Si MAS NMR spectra.

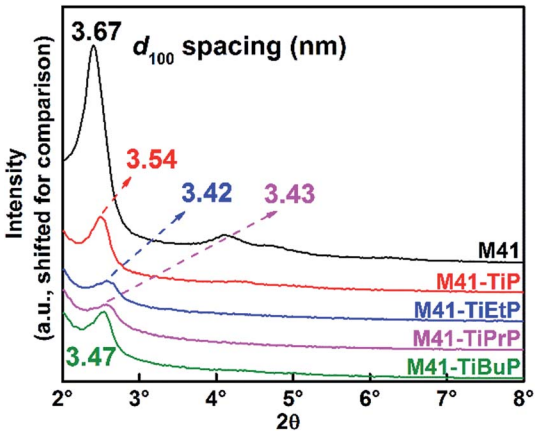

Fig. 2 XRD patterns ($2\theta = 2–8°$) of the synthesised materials.

to longitudinal and transversal optic of the asymmetric stretching vibrations of the siloxane groups. The peak at about 800 cm^{-1} can be assigned to the symmetric stretching vibration of the same group. The shoulder peak at 970–980 cm^{-1} is attributed to the Si–O^- stretching vibration of the silanol group.[33] The peaks centred at 750 cm^{-1} are only visible from the alkyl-grafted materials. It is due to the asymmetric P–O–C stretching vibration,[34] confirming the successful grafting process.

The deconvoluted ^{29}Si magic-angle spinning nuclear magnetic resonance (MAS NMR) spectra of these materials (Fig. 3) show in general three peaks at −92, −101 and −110 ppm corresponding to geminal silanol ($(SiO)_2$*$Si(OH)_2$, Q^2 site), isolated silanol ($(SiO)_3$*SiOH, Q^3 site) and framework silicon sites ($(SiO)_4$*Si, Q^4 site).[35] Ti is considered isomorphic with Si and therefore the substitution of Si by Ti does not result in distinguishable changes in ^{29}Si resonance. Approximately 40% of the silicon are in surface silanol groups ($Q^2 + Q^3$). A general trend of the decrease in Q^2 and Q^3 resonances as well as the increase in Q^4 resonance is shown in Table 1. This intensity redistribution is a strong indication for surface modification of the silanol groups by titanium derivatives.

The ^{31}P MAS NMR spectra of the synthesised materials are shown in Fig. 4. The spectra were assigned based on literature data[36] and the relative content of different P species are listed in Table 2. The phosphate groups were linked not only to surface titanol but to silanol groups as well. Approximately 40% of the P species were surface titanium(IV) (alkyl)phosphates (3, 4, 6) and 30–49% were surface silicon (alkyl)phosphates (1, 2, 5). The titanium(IV) hydrogenphosphate (7) and pyrophosphate (8), representing the remaining 20% P species, most probably existed in quasi-amorphous state rather than being covalently linked to the surface.[36] The results indicated that the phosphate grafting rate was higher for titanium(IV) than silicon, since the overall surface silanol groups were more abundant than titanol groups according to the elemental analysis and ^{29}Si NMR spectra. Therefore, the titanium(IV) layer enhanced the degree of functionalisation of the material.

The grafting of organic moieties was investigated by two other methods. Solid-state ^{1}H–^{13}C cross polarisation (CP)/MAS NMR spectra in Fig. 5 show peaks corresponding to grafted alkyl chains. For instance, in the M41-TiPrP sample, the peak at 60–70 ppm represents the first carbon atom (a) of the *n*-propyl group, while the peak at 25 and 10 ppm indicate the middle (b) and terminal (c) carbon atoms, respectively. The overlapping peaks are caused by the fact that some alkylphosphate groups are attached to Ti atoms and some to Si atoms.

Thereafter, simultaneous thermogravimetry and differential scanning calorimetry-mass spectroscopy (TG/DSC-MS) was utilised to study the thermal decomposition behaviour of the grafted materials. Fig. 6 illustrates the ion intensity profile of selected *m*/*z* values representing ethylene, propene, butene and CO_2 with increasing temperature. The grafted *n*-alkyl chains started to decompose at approximately 200 °C *via cis*-elimination to produce acids and alkenes.[37] The reaction mechanism in

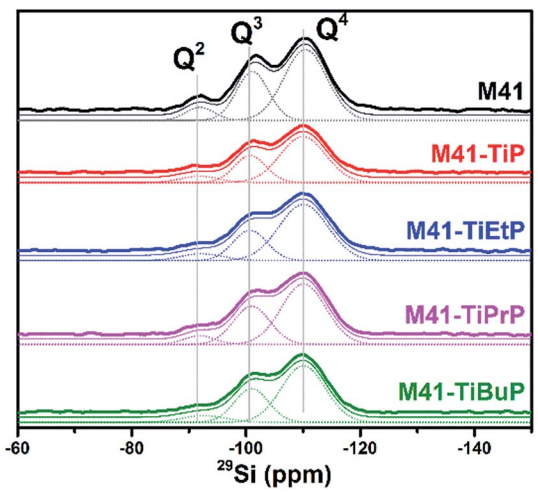

Fig. 3 Solid-state ^{29}Si MAS NMR spectra of the synthesised materials with peak deconvolutions.

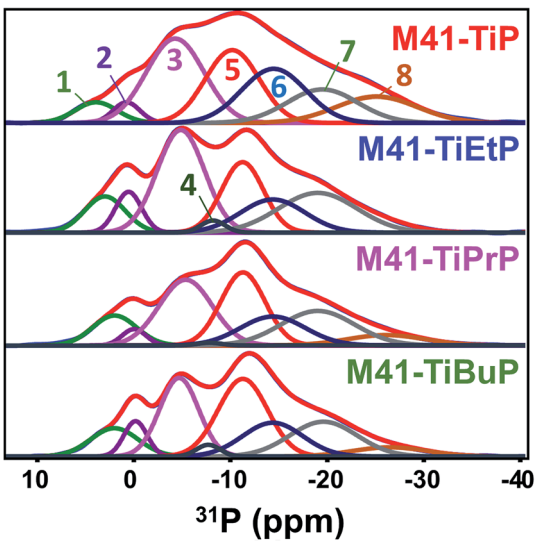

Fig. 4 ^{31}P MAS NMR spectra with peak deconvolutions (numbers representing peak assignments are listed in Table 2).

Table 2 Assignments and relative quantification of P species from ^{31}P MAS NMR spectra (R = H, Et, *n*-Pr or *n*-Bu)

		Relative quantification (%)			
Position *ca.* (ppm)	Species (peak number in Fig. 4)	M41-TiP	M41-TiEtP	M41-TiPrP	M41-TiBuP
0 and 2	≡SiO-PO(OR)$_2$ (1,2)	8	16	13	15
−5 and −7.5	≡TiO-PO(OR)$_2$ (3,4)	27	31	26	23
−11	(≡SiO)$_2$-PO-(OR) (5)	21	18	23	27
−14.5	(≡TiO)$_2$-PO-(OR) (6)	19	13	14	14
−19	Ti(HPO$_4$)$_2$ (7)	13	19	18	16
−26	TiP$_2$O$_7$ (8)	12	3	6	5

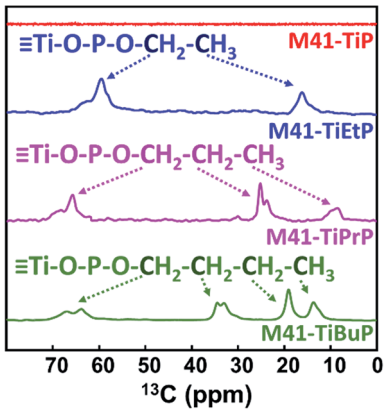

Fig. 5 Solid-state ^{1}H–^{13}C CP/MAS NMR spectra of the synthesised materials.

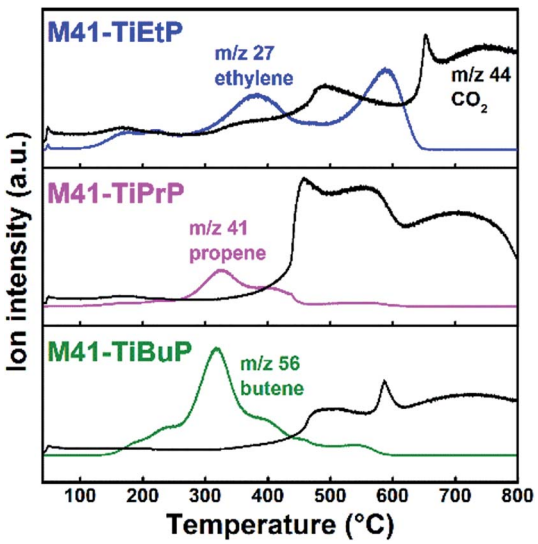

Fig. 6 TG/DSC-MS profiles showing ion intensities corresponding to the evolved ethylene, propene, butene and CO_2.

producing butene is demonstrated in Scheme 2. The produced alkene subsequently reduced phosphate and silica, thereby CO_2 was emitted in all the samples at temperature more than 400 °C. The entire TG/DSC-MS profiles are given in Fig. S3–S5.†

The overall characterisation suggested that the short *n*-alkyl chains were successfully grafted onto the M41-TiP material.

Scheme 2 Thermal decomposition of surface titanium *n*-butyl phosphate *via* a *cis* elimination mechanism.

However, it was not possible to fully functionalise all the surface silanol groups with Ti. Due to the differences in reaction activity and diffusion resistance of the alcohols, the degree of organic grafting differed and was not easily quantifiable. The mesoporous nature of the M41 silica support also resulted in residual acetone and pyridine left inside the final products. Even after treatment in a vacuum oven at 50 °C for 2 days, it was not possible to remove them until below the detection limit.

Batch uptake of scandium and lanthanum

Batch sorption studies were conducted to evaluate the uptake behaviour of different rare-earth ions on the synthesised hybrid materials. Among all the REEs, scandium is the lightest element and is almost always found in minerals together with yttrium and lanthanides. The uptake of scandium and lanthanides in their mixture could indicate the potential of separating them. To simplify the situation, lanthanum is used as a representative lanthanide here. Due to the solvating extraction nature of the prepared sorbents, batch uptake experiments were conducted in aqueous solutions with and without 5 M NH_4NO_3 as the nitrate ion supply.

The values for distribution coefficients (K_d) of scandium and lanthanum along with their calculated separation factors are plotted in Fig. 7. In our adopted system, a K_d value of 400 would mean 50% uptake and a K_d value of 3600 indicated 90% uptake. In Fig. 7a, the K_d values for Sc increased with elevated pH throughout the investigated pH range (1.5 to 4) for the pristine M41 and M41-TiP. These materials also exhibited lower scandium uptake when 5 M NH_4NO_3 was present in the solution. Presumably, only ion-exchange and physisorption sites were accounted for the uptake and the addition of competing cations resulted in lower uptake. For the hybrid materials, the situation was reversed. Higher scandium uptake was obtained under the

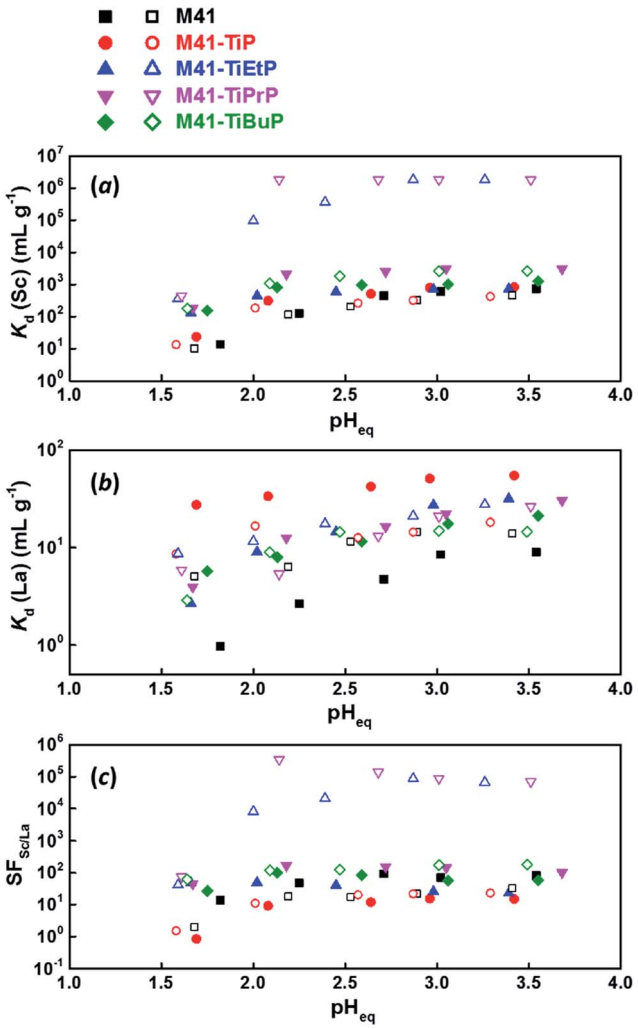

Fig. 7 K_d values for scandium (a) and lanthanum (b) and the corresponding $SF_{Sc/La}$ values (c) as a function of equilibrium pH for sorption systems with 5 M NH_4NO_3 (open symbols) and without NH_4NO_3 (closed symbols). Initial solution composition: 1 mM Sc and 1 mM La, sorption solid-to-liquid ratio: 50 mg/20 mL.

presence of additional nitrate ions. Note that nearly all the scandium in the solution was taken up by M41-TiEtP and M41-TiPrP in the pH range of 2 to 4, translating into K_d values more than 10^6 mL g^{-1}. The lanthanum uptake was suppressed in this system, resulting in lesser K_d values ranging from 1 to 100 mL g^{-1} (Fig. 7b).

In view of the separation factors for scandium and lanthanum ($SF_{Sc/La}$, in Fig. 7c), scandium was clearly favoured by all the materials and the separation factors in the magnitudes of 10 to 100 were achieved using inorganic M41 and M41-TiP. Notably, separation factors over 100 000 were obtained for M41-TiEtP and M41-TiPrP under 5 M NH_4NO_3 condition. This demonstrates the excellent potential of the hybrid materials in the separation of scandium and lanthanides. In SX operations, triethyl phosphate and tri-*n*-propyl phosphate are in general not used due to their higher solubility in the aqueous phase. However, their solvating behaviour towards REE nitrate complexes are similar compared to that of TBP. When the alkyl chains are immobilised on a solid surface, their solubility in water is no longer an issue. The reason why M41-TiEtP and M41-TiPrP outperformed M41-TiBuP is very likely due to the higher organic loading in the two former materials.

Batch uptake of lanthanides

The SPX capabilities of the synthesised grafted materials towards lanthanides were evaluated by batch sorption experiments using a binary 1 mM equimolar neodymium and dysprosium mixture with 5 M NH_4NO_3. Here, neodymium represented the light REEs and dysprosium represented the heavy REEs. This lanthanide pair was selected also due to its industrial relevance (recycling of NdFeB magnets). High concentrations of nitrate ions were used because of the solvating extractant nature of TBP. As demonstrated earlier, a very small amount of lanthanum was adsorbed on M41 and M41-TiP. Similarly, the results in Fig. 8a indicate that the M41 silica support and M41-TiP exhibited negligible total neodymium and dysprosium uptake, while the M41-TiEtP, M41-TiPrP and M41-TiBuP showed a significant uptake (0.12, 0.34 and 0.25 mmol g^{-1}, respectively) at an equilibrium pH of approximately 2. Comparable behaviour has been observed in uranyl sorption by phosphoryl and phosphoryl-ether-functionalised metal–organic framework, where the uptake was much higher in the ethoxy-protected materials rather than the phosphoric acid analogues.[38] In our cases, the differences in uptake among the hybrid materials originated from the variations in the degree of surface functionalisation by alkyl groups and from the differences in the stability of the ternary lanthanide–nitrate–alkyl-phosphate complexes.[9]

The K_d for neodymium and dysprosium were calculated at different equilibrium pH conditions in M41-TiPrP sample and shown in Fig. 8c. The separation factors for dysprosium/neodymium ($SF_{Dy/Nd}$) were approximately 3 in all tested pH conditions. This is comparable with a solvent extraction system using TBP in benzene with 6 M NH_4NO_3, where the distribution ratio obtained for neodymium is 0.029 and for dysprosium is 0.081,[39] thus resulting in a $SF_{Dy/Nd}$ of 2.8. The K_d and $SF_{Dy/Nd}$ values of M41-TiEtP and M41-TiBuP are given in Fig. 8b and d. The increase in equilibrium pH increased both K_d values and had only a limited impact on the $SF_{Dy/Nd}$. The decrease in lanthanide uptake with increasing acidity is likely due to the competitive co-extraction of HNO_3.[40]

The desorption process was almost quantitative when using a 0.1 M HNO_3 solution (Fig. S6†), in which H^+ inhibited the residual ion exchange sites (silanol and titanol) and low nitrate concentration favoured the breakdown of lanthanide nitrate complexes. Cyclic sorption–desorption tests (five cycles, Fig. S7†) confirmed the reusability of our prepared hybrid sorbents. The SF(Dy/Nd) values remained stable throughout the five adsorption cycles. Further column tests are needed to investigate the extraction and stripping behaviour (including kinetics) under extraction conditions.

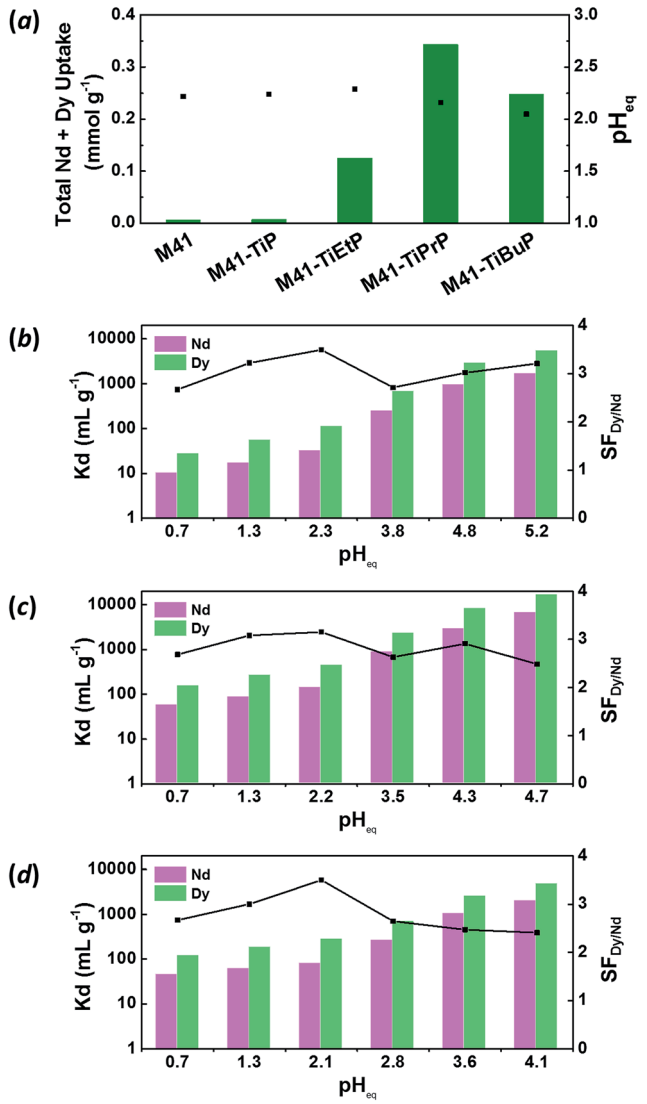

Fig. 8 (a) Total Nd and Dy uptake (bars) of five synthesised materials and their corresponding equilibrium pH values (squares), K_d values (bars) and $SF_{Dy/Nd}$ (squares) as a function of equilibrium pH for (b) M41-TiEtP, (c) M41-TiPrP and (d) M41-TiBuP material. Initial solution composition: 1 mM Nd, 1 mM Dy and 5 M NH_4NO_3, sorption solid-to-liquid ratio: 50 mg/20 mL.

Stability towards strong acids

One major drawback of siliceous materials is their poor stability in strongly acidic solutions.[20] This hinders their application in hydrometallurgical conditions. It is known that titanium(IV) oxides and phosphates are less soluble in acidic media and therefore functionalisation of silica with titanium(IV) derivatives should lead to enhanced acid stability.[41] The reason that mesoporous titanium materials are not directly utilized for synthesis is because of comparatively difficult and unreproducible control over the synthesis. Table 3 summarises the amount and relative percentage of dissolved silicon and titanium in nitric acid solutions. More than 5% of the silica in M41 silica was dissolved in our batch system under 0.1 M HNO_3 solution. Functionalisation with titanium phosphate led to apparent improvement in acid stability, with less than 0.6% of the silica from M41-TiP dissolved under the same condition. Notably, alkyl grafting further enhanced the acid stability of the materials most likely due to increased hydrophobicity.

Table 3 Acid stability of the pristine and the grafted M41 materials[a]

	0.1 M HNO_3 (pH 1)				0.01 M HNO_3 (pH 2)			
	Dissolved[b] Si		Dissolved Ti		Dissolved Si		Dissolved Ti	
Materials	ppm	%	ppm	%[c]	ppm	%	ppm	%
M41	62.31	5.34%	—	—	21.9	1.88%	—	—
M41-TiP	6.15	0.53%	0.16	0.08%	3.71	0.32%	N.D.[d]	N.D.
M41-TiEtP	4.27	0.37%	0.08	0.04%	3.91	0.34%	N.D.	N.D.
M41-TiPrP	5.18	0.44%	0.12	0.06%	3.52	0.30%	N.D.	N.D.
M41-TiBuP	3.19	0.27%	0.09	0.05%	2.66	0.23%	N.D.	N.D.

[a] Batch solid-to-liquid ratio: 50 mg/20 mL acid, contact time: 6 h. [b] Passed through 0.45 μm syringe filter. [c] Percentage calculated based on elemental analysis results. [d] Not detectable (<0.01 ppm).

Mechanistic consideration of uptake and selectivity

The prepared hybrid sorbents (M41-TiEtP, M41-TiPrP and M41-TiBuP) have different sorption sites for the uptake of rare-earth ions. First of all, the remaining silanol (–SiOH), titanol (–TiOH) and hydrogen phosphate groups (–HPO_4) have hydroxyl groups serving as cation-exchange sites. Secondly, the mesostructured materials have large surface areas, which accounts for the physisorption. Finally and most importantly, the grafted alkylphosphate groups act as solvating extractants that are capable of immobilising the neutral rare-earth nitrate complexes by donating electrons. Ion-exchange and physisorption are inhibited by the addition of ammonium nitrate (NH_4^+ to compete with cation exchange sites). On the other hand, the solvating extraction behaviour is enhanced through the formation of rare-earth nitrate complexes.

Scandium and lanthanides are hard Lewis acids and phosphates are hard Lewis bases. The affinity of hard acids to hard bases are mostly ionic in nature. The ionic radius of scandium (74.5 pm, 6-coordinate) is smaller than that of the lanthanides (103.2 to 121.6 pm, 9-coordinate from the series La^{3+} to Lu^{3+}),[42] therefore scandium is a stronger Lewis acid and forms more stable coordination bond with phosphate (containing hard-atom O).

For the hybrid sorbents, based on the electronic effect, titanium atoms and the alkyl chains both donate electrons to the attached phosphoryl group (P=O), thereby increasing the electron density on the oxygen atom. The resulting titanium(IV) alkylphosphates are even stronger Lewis bases than TBP and inorganic phosphate, respectively. Therefore, a stronger Lewis acid with a small ionic radius is favoured and thus resulting in the enhanced uptake and the selectivity of Sc^{3+} over La^{3+}. Due to lanthanide contraction, the ionic radius of Dy^{3+} is smaller than that of Nd^{3+} and subsequently Dy^{3+} is better retained by the hybrid materials. By selecting the metal which links the silica and the organophosphate group and by using different types of

organophosphorus moieties, it is possible to further fine-tune the basicity of the phosphoryl ligands.

The length of the alkyl chains should affect the molecular recognition events (size-exclusion preferences) and the attachment of the alkyl chains to the solid matrix surface potentially adds to the overall rigidity of the complex. However, this behaviour cannot be fully elucidated in the current situation since the amounts of grafted alkyl chains vary for the different alkyl chains.

Conclusions

We have demonstrated the feasibility of designing a hybrid composite material mimicking the structure of organophosphate solvent extractants. Mesoporous silica offers a high surface area for heteroatom functionalisation and improved contact efficiency with aqueous solutions. A metal(IV) phosphate acts as a versatile acid-resistant platform for grafting of organic chains *via* a Ti(IV)–O–P bond. Our approach is different from the conventional organic grafting route where silylation reagents containing the extractant structure were employed. The synthesised M41 silica grafted titanium(IV) alkylphosphate hybrid materials mimicking the TBP structure showed excellent scandium and lanthanum separation potential from nitrate feed solution. These materials also presented intra-lanthanide separation capabilities comparable to that of TBP in SX systems. Our proposed idea can be utilised for obtaining task-specific materials, *e.g.* covalently anchoring of longer organic chains (mimicking the DEPHA, bis(2-ethylhexyl) phosphate, structure), which are more selective for intra-lanthanide separations. Alternatively, phosphonates and phosphinates can be synthetically introduced as metal(IV) derivatives, allowing precisely tuned selectivity. The knowledge gained from SX systems is transferable, to a certain extent, to guide the future design of hybrid materials for rare-earth separations by the SPX mechanism.

Conflicts of interest

There are no conflicts to declare.

Acknowledgements

The research leading to these results has received funding from the European Community's Horizon 2020 Programme under Grant Agreement no. 636876 (MSCA-ETN REDMUD). Dr Sambhu Radhakrishnan and Dr Eric Breynaert (KU Leuven) are thanked for performing the solid-state ^{13}C and ^{31}P NMR measurements. Bart Van Huffel, Dirk Henot (KU Leuven) and Pasi Heikkilä (University of Helsinki) are acknowledged for BET, CHN and XRD analysis, respectively.

Notes and references

1 K. Binnemans, P. T. Jones, B. Blanpain, T. Van Gerven, Y. Yang, A. Walton and M. Buchert, *J. Cleaner Prod.*, 2013, **51**, 1–22.
2 J. Florek, D. Larivière and F. Kleitz, in *Nanotechnology: Delivering on the Promise Volume 2*, American Chemical Society, 2016, vol. 1224, ch. 6, pp. 107–117.
3 F. Xie, T. A. Zhang, D. Dreisinger and F. Doyle, *Miner. Eng.*, 2014, **56**, 10–28.
4 B. Kronholm, C. G. Anderson and P. R. Taylor, *JOM*, 2013, **65**, 1321–1326.
5 T. Vander Hoogerstraete, S. Wellens, K. Verachtert and K. Binnemans, *Green Chem.*, 2013, **15**, 919–927.
6 A. G. Baldwin, N. J. Bridges and J. C. Braley, *Ind. Eng. Chem. Res.*, 2016, **55**, 13114–13119.
7 S. Mishra, J. Dwivedi, A. Kumar and N. Sankararamakrishnan, *New J. Chem.*, 2016, **40**, 1213–1221.
8 E. Hesford, E. Jackson and H. McKay, *J. Inorg. Nucl. Chem.*, 1959, **9**, 279–289.
9 C. Kalaya and C. Deacha, *J. Rare Earths*, 2011, **29**, 896–901.
10 C. Siva Kesava Raju and M. S. Subramanian, *J. Hazard. Mater.*, 2007, **145**, 315–322.
11 V. Luca, J. J. Tejada, D. Vega, G. Arrachart and C. Rey, *Inorg. Chem.*, 2016, **55**, 7928–7943.
12 J. Florek, S. Giret, E. Juere, D. Lariviere and F. Kleitz, *Dalton Trans.*, 2016, **45**, 14832–14854.
13 J. Veliscek-Carolan, T. L. Hanley and V. Luca, *Sep. Purif. Technol.*, 2014, **129**, 150–158.
14 R. Silbernagel, C. H. Martin and A. Clearfield, *Inorg. Chem.*, 2016, **55**, 1651–1656.
15 W. Zhang, G. Ye and J. Chen, *J. Mater. Chem. A*, 2013, **1**, 12706–12709.
16 P. J. Lebed, K. de Souza, F. Bilodeau, D. Lariviere and F. Kleitz, *Chem. Commun.*, 2011, **47**, 11525–11527.
17 T. Ogata, H. Narita and M. Tanaka, *Hydrometallurgy*, 2015, **155**, 105–109.
18 P. J. Lebed, J.-D. Savoie, J. Florek, F. Bilodeau, D. Larivière and F. Kleitz, *Chem. Mater.*, 2012, **24**, 4166–4176.
19 J. A. Shusterman, H. E. Mason, J. Bowers, A. Bruchet, E. C. Uribe, A. B. Kersting and H. Nitsche, *ACS Appl. Mater. Interfaces*, 2015, **7**, 20591–20599.
20 J. Shusterman, H. Mason, A. Bruchet, M. Zavarin, A. B. Kersting and H. Nitsche, *Dalton Trans.*, 2014, **43**, 16649–16658.
21 J. Florek, F. Chalifour, F. Bilodeau, D. Larivière and F. Kleitz, *Adv. Funct. Mater.*, 2014, **24**, 2668–2676.
22 E. Juere, J. Florek, D. Lariviere, K. Kim and F. Kleitz, *New J. Chem.*, 2016, **40**, 4325–4334.
23 A. I. Bortun, L. N. Bortun, A. Clearfield, S. A. Khainakov, V. V. Strelko, V. N. Khryashevskii, A. P. Kvashenko and I. I. Voitko, *Solvent. Extr. Ion. Exc.*, 1997, **15**, 515–532.
24 W. Zhang, R. Koivula, E. Wiikinkoski, J. Xu, S. Hietala, J. Lehto and R. Harjula, *ACS Sustainable Chem. Eng.*, 2017, **5**, 3103–3114.
25 G. E. Fryxell, H. Xu, Y. Lin, W. J. Shaw, J. C. Birnbaum, J. C. Linehan, Z. Nie, K. Kemner and S. Kelly, *J. Mater. Chem.*, 2004, **14**, 3356–3363.
26 M. Grün, K. K. Unger, A. Matsumoto and K. Tsutsumi, *Microporous Mesoporous Mater.*, 1999, **27**, 207–216.

27 J. Zhang, Z. Ma, J. Jiao, H. Yin, W. Yan, E. W. Hagaman, J. Yu and S. Dai, *Microporous Mesoporous Mater.*, 2010, **129**, 200–209.
28 F. Hoffmann, M. Cornelius, J. Morell and M. Fröba, *Angew. Chem., Int. Ed.*, 2006, **45**, 3216–3251.
29 J. Zhang, Z. Ma, J. Jiao, H. Yin, W. Yan, E. W. Hagaman, J. Yu and S. Dai, *Langmuir*, 2009, **25**, 12541–12549.
30 A. Styskalik, D. Skoda, Z. Moravec, J. G. Abbott, C. E. Barnes and J. Pinkas, *Microporous Mesoporous Mater.*, 2014, **197**, 204–212.
31 G. Cao, H. G. Hong and T. E. Mallouk, *Acc. Chem. Res.*, 1992, **25**, 420–427.
32 Q. Cai, W.-Y. Lin, F.-S. Xiao, W.-Q. Pang, X.-H. Chen and B.-S. Zou, *Microporous Mesoporous Mater.*, 1999, **32**, 1–15.
33 L. Liu, D. K. Wang, D. L. Martens, S. Smart, E. Strounina and J. C. D. da Costa, *RSC Adv.*, 2014, **4**, 18862–18870.
34 G. Socrates, *Infrared and Raman characteristic group frequencies: tables and charts*, John Wiley & Sons, New York, 2004.
35 X. Zhao, G. Lu, A. Whittaker, G. Millar and H. Zhu, *J. Phys. Chem. B*, 1997, **101**, 6525–6531.
36 T. Kovalchuk, H. Sfihi, A. Korchev, A. Kovalenko, V. Il'in, V. Zaitsev and J. Fraissard, *J. Phys. Chem. B*, 2005, **109**, 13948–13956.
37 S. Gaan, G. Sun, K. Hutches and M. H. Engelhard, *Polym. Degrad. Stab.*, 2008, **93**, 99–108.
38 M. Carboni, C. W. Abney, S. Liu and W. Lin, *Chem. Sci.*, 2013, **4**, 2396–2402.
39 M. Majdan, *Hydrometallurgy*, 1994, **35**, 179–185.
40 T. Vander Hoogerstraete and K. Binnemans, *Green Chem.*, 2014, **16**, 1594–1606.
41 M. Shahadat, T. T. Teng, M. Rafatullah and M. Arshad, *Colloids Surf., B*, 2015, **126**, 121–137.
42 R. Shannon, *Acta Crystallogr., Sect. A: Cryst. Phys., Diffr., Theor. Gen. Crystallogr.*, 1976, **32**, 751–767.

